

## Article

# Intermittent Beginning to the Formation of Hydrogenous Ferromanganese Nodules in the Vast Field: Insights from Multi-Element Chemostratigraphy Using Microfocus X-ray Fluorescence

Shiki Machida <sup>1,2,\*</sup> , Ryo Shimomura <sup>3</sup>, Kentaro Nakamura <sup>1,3</sup>, Tetsu Kogiso <sup>4</sup>  and Yasuhiro Kato <sup>1,2,3</sup>

<sup>1</sup> Ocean Resources Research Center for Next Generation (ORCeNG), Chiba Institute of Technology, Chiba 275-0016, Japan; kentaron@sys.t.u-tokyo.ac.jp (K.N.); ykato-ecc@g.ecc.u-tokyo.ac.jp (Y.K.)

<sup>2</sup> Frontier Research Center for Energy and Resources (FRCER), School of Engineering, The University of Tokyo, Tokyo 113-8656, Japan

<sup>3</sup> Department of Systems Innovation, School of Engineering, The University of Tokyo, Tokyo 113-8656, Japan; rshimomura58@gmail.com

<sup>4</sup> Graduate School of Human and Environmental Studies, Kyoto University, Kyoto 606-8501, Japan; kogiso.tetsu.6s@kyoto-u.ac.jp

\* Correspondence: shiki.machida@p.chibakoudai.jp; Tel.: +81-47-478-0183



**Citation:** Machida, S.; Shimomura, R.; Nakamura, K.; Kogiso, T.; Kato, Y. Intermittent Beginning to the Formation of Hydrogenous Ferromanganese Nodules in the Vast Field: Insights from Multi-Element Chemostratigraphy Using Microfocus X-ray Fluorescence. *Minerals* **2021**, *11*, 1246. <https://doi.org/10.3390/min11111246>

Academic Editor: Georgy Cherkashov

Received: 22 September 2021

Accepted: 7 November 2021

Published: 10 November 2021

**Publisher's Note:** MDPI stays neutral with regard to jurisdictional claims in published maps and institutional affiliations.



**Copyright:** © 2021 by the authors. Licensee MDPI, Basel, Switzerland. This article is an open access article distributed under the terms and conditions of the Creative Commons Attribution (CC BY) license (<https://creativecommons.org/licenses/by/4.0/>).

**Abstract:** Vast ferromanganese nodule fields have been found on the deep-sea floor of all oceans worldwide. They have received attention because they potentially provide high-grade metal resources to develop future high- and green-technology. However, how these vast nodule fields were formed and developed owing to their widespread nature or tendency to be denser with an increasing number of nodules has not yet been established. In this study, the fine-scale inner structure of nodules of various sizes was analyzed on the basis of chemical mapping using microfocus X-ray fluorescence. We found that nodules distributed in the vast field around Minamitorishima (Marcus) Island have several types of innermost layers, which correspond to different chemostratigraphic layers of nodules that have been previously reported by us in this region. As nodules grow in order from the center to the outside, the different types in the innermost layer indicate a difference in the timing of the beginning of their growth. Moreover, because the differences in the chemical features of each layer reflect differences in the composition of the original deep-sea water, our results imply that the beginning of nodule formation occurred intermittently at each time of a water mass replacement due to new deep-sea currents flowing into this region. We recognized that the northern part of the study area was dominated by large nodules that started to grow in relatively earlier times, while the southern part tended to have many nodules that grew in relatively later times. Based on these observations, we hypothesize that the intermittent beginning of nodule formation is governed by the northward inflow of the deep-sea current that originated from the Lower Circumpolar Deep Water for an extended time to form the vast nodule field. Because patterns in the timing of nodule formation were different in the eastern and western regions, we thus further propose that the topographic framework, i.e., the arrangement of individual large seamounts and the cluster of small knolls and petit-spot volcanoes, strongly regulates the flow path of the deep-sea current, even if the position of the entire seamount changes owing to plate motion. The deep-sea current might supply some materials to be nuclei, resulting in the nodule formation at the beginning of the process.

**Keywords:** ferromanganese nodule;  $\mu$ -XRF; Minamitorishima Island; deep-sea current; Pacific Ocean circulation; the lower circumpolar deep water

## 1. Introduction

Ferromanganese nodules are considered a prospective resource for critical metals, particularly for Co, Ni, Mo, W and rare-earth elements. Large nodule fields have been found

in the Clarion–Clipperton Zone, the Peru and Penrhyn–Samoa Basins, the region around Minamitorishima (Marcus) Island in the Pacific Ocean, and the Central Indian Ocean basin [1–5]; However, the mechanism of the formation of these vast nodule fields has not been elucidated. Although several styles of the grain size distribution (e.g., homogeneous or bimodal) for the dense nodule field were observed [5–10], the critical factor has not yet been constrained.

The Japanese exclusive economic zone (EEZ) surrounding Minamitorishima Island (Figure 1), hereafter referred to as the Minamitorishima EEZ, is located on the northern margin of the Prime Crust Zone in the western Pacific [11,12]. The Minamitorishima EEZ is considered to be one of the most prospective areas of the field that is densely covered by hydrogenous ferromanganese nodules [3]. Recent fine-scale chemostratigraphic observations on the basis of microfocus X-ray fluorescence ( $\mu$ -XRF) mapping of the entire cross-section of hydrogenous nodule samples [13] revealed that Fe, Mn, and Ti distributions represent major oxide or oxyhydroxide phases. On the other hand, the distribution of P, Si, and Cu represent the contribution of biogenic or pelagic sediment components filling the non-oxide and -oxyhydroxide portions. Based on these chemical fingerprints, it has been demonstrated that element(s) characterizing the individual ferromanganese layers of nodules can be visualized by a “multichemical feature map” which is constructed by merging the compositional maps for Fe, Mn, Ti, P, Si, and Cu into a single map. While identifying each layer using a multichemical feature map it was evident that a general pattern of the layer structure, forming nine chemically characteristic layers, was common throughout the growth history of the nodules in the entire regions of Minamitorishima EEZ [13]. As discussed by Machida et al. [14], the structure of the ferromanganese layers of nodules in the Minamitorishima EEZ is the same as that of the ferromanganese crust on seamounts or knolls in the Prime Crust Zone [15–19]. This implies that a common deep-sea water mass had contributed to the formation of hydrogenous nodules and crusts across a vast region of the western Pacific. Currently, the Lower Circumpolar Deep Water (LCDW), flowing through the southern edge of the Minamitorishima EEZ region, acts as the western branch current of the Deep Western Boundary Current (DWBC) (Figure 1) [20–22]. Although the main DWBC flows into the region from the southern direction and flows out in the northwest, descendent flow is expected to pass through the area from the south to the north. In this study, we evaluated whether the water-mass transformation history of the LCDW can be represented as the structural change of ferromanganese nodules in this region.

A recent exhaustive structural analysis of nodules collected from the Minamitorishima EEZ using X-ray computed tomography (CT) revealed that the size of nodules is regulated by the total thickness of the ferromanganese layers of the nodules [23]. This leads us to consider that, if we can identify the innermost layer (i.e., the layer around the nuclei) of each different-sized nodule using the multichemical feature map, we can examine the relationship between the timing of initiation of nodule formation and the water-mass transformation history of the DWBC in this region. Here, we report the results of  $\mu$ -XRF mapping of the cross-section of nodule samples covering the observed size variation around Minamitorishima Island. Based on the results, we discuss the causality of the beginning of nodule formation in terms of deep-sea currents to form the vast nodule field around Minamitorishima Island.

## 2. Materials and Methods

### 2.1. General Description of the Sampling Sites

The samples analyzed in this study were collected during seven dives of the submersible *SHINKAI 6500* during cruise YK16-01 of the *R/V Yokosuka* in the Minamitorishima EEZ (Figures 1 and 2) [3,13]. The 6K#1459, 6K#1462 and 6K#1463 dives sampled from the nodule-dense area (i.e., high acoustic backscatter intensity area), which lies near the eastern to southeastern edge of the EEZ, hereafter are referred to as the “East EEZ region” and “Southeast EEZ region” as according to Machida et al. [13]. In contrast, the 6K#1460, 6K#1461, 6K#1464

and 6K#1465 dives sampled from the nodule-dense area of the eastern to southeastern region of the Takuyo Daigo seamount are hereafter referred to as “Around Takuyo Daigo Seamount region” as according to Machida et al. [13]. As described in the following section, we covered representative samples with various layer thicknesses collected from each site. The size of the nodules was described on board, where Max.: maximum length, Med.: medium length, and Min.: minimum length (Table 1). In the following sections, we summarize the results obtained during dives at individual areas and the structure of the samples obtained in this study.

#### 2.1.1. East and Southeast EEZ Regions

Areas of high acoustic backscatter intensity are widely distributed in the East and Southeast EEZ regions [5]. Our submersible observations indicate that these represent fields densely covered by ferromanganese nodules. Most of the sampling sites, except for stop 5 of the 6K#1459 dive and stop 4 of the 6K#1463 dive, are classified as Type-H or Type-V facies, which are characterized by high to almost complete coverage by rounded nodules [5]. The other areas were classified as Type-L (stop 5 of the 6K#1459 dive) or Type-M (stop 4 of the 6K#1463 dive) facies, which are characterized by coverage of smaller nodules compared to those in the areas classified as Type-H or Type-V facies [5] (Table 1). Although smaller nodules are also distributed in the areas classified as Type-H or Type-V facies, no small samples were recovered at stops 1–3 of the 6K#1459 dive, the reason for which is because we could not use a scoop for sampling [23].

At Site 6K#1462, there was relatively minor change in the water depth along the dive track (Table 1 and Figure 2). In contrast, during dives 6K#1459 and 6K#1463, variable water depths were observed along the track (Figure 2). In the case of dive 6K#1459, we observed that only small nodules were distributed at deeper parts of the slope of the knoll (stop 5; Table 1 and Figure 2). This is in contrast to dive 6K#1463, where the shallower part of the knoll slope was covered exclusively by small nodules (Table 1 and Figure 2).

#### 2.1.2. Around Takuyo Daigo Seamount Region

Areas of high acoustic backscatter intensity, representing the fields densely covered by ferromanganese nodules, are distributed particularly from east to south of the Takuyo Daigo seamount [5]. Most of the sampling sites, except for stops 1 and 2 of the 6K#1461 dive and stop 4 of the 6K#1465 dive, are classified as Type-H or Type-V facies [5]. Such regions are characterized by high to almost complete coverage by rounded nodules. The areas classified as Type-L facies (stops 1 and 2 of the 6K#1461 dive) and Type-M facies (stop 4 of the 6K#1465 dive) are sparsely covered by small and large nodules, respectively (Table 1). Although small nodules are also distributed in the areas classified as Type-H or Type-V facies, no small samples were recovered at stops 1 and 2 of the 6K#1460 dive. This is because we could not use a scoop for sampling [23], due to strong anchoring of the nodules to the below sediment.

In the Around Takuyo Daigo Seamount region, there is only a minor change in water depth along the dive tracks (Table 1 and Figure 2). Moreover, as demonstrated by Machida et al. [5], we did not observe any systematic correlation between the topographic features (i.e., moat or mound) and distribution density or size variation of the nodules.

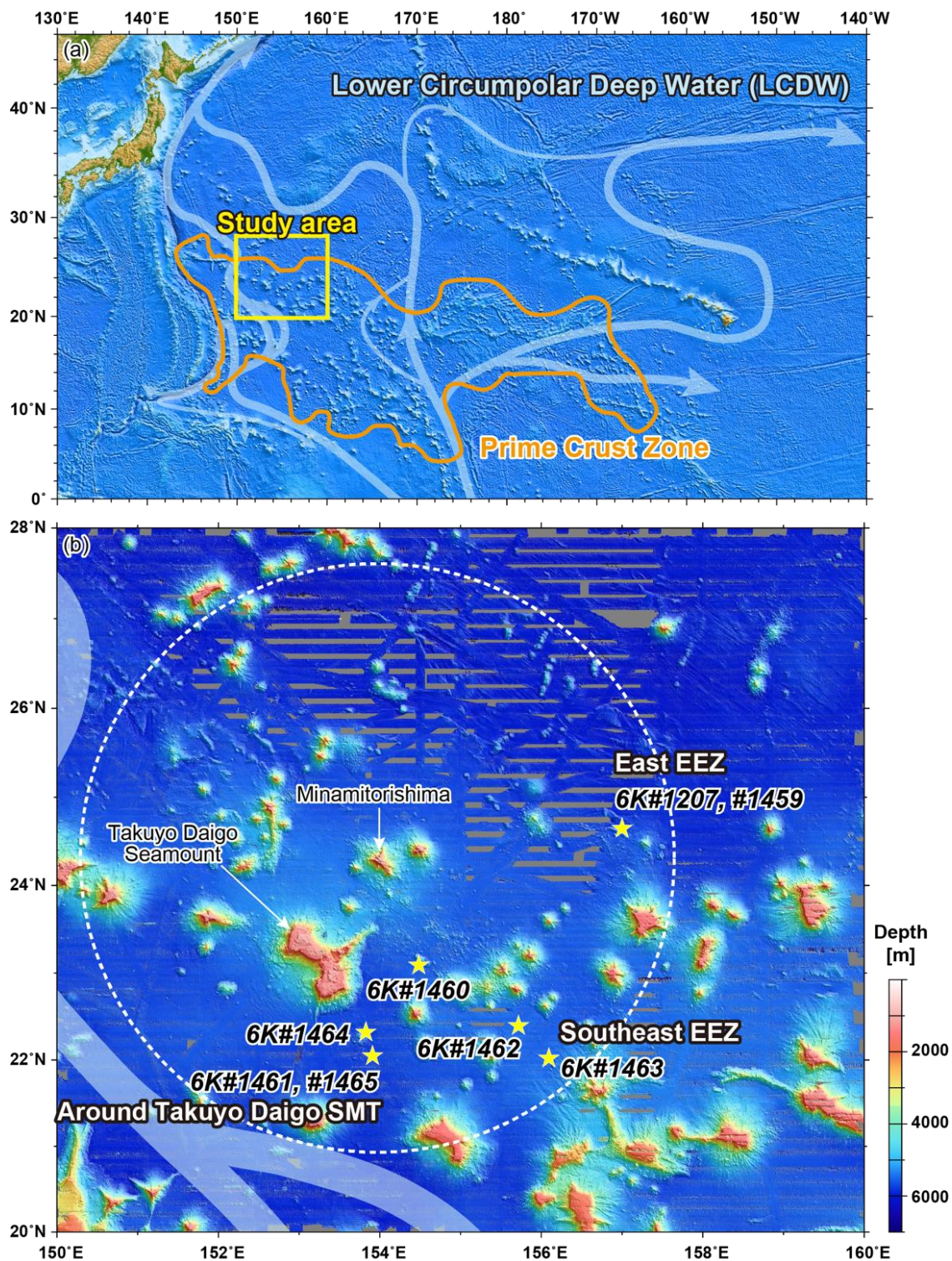


**Figure 1.** Topography of the regions surrounding the Minamitorishima island. (a) Light blue arrows indicate the present circulation of the Pacific Ocean in the lower deep layer originated from the Lower Circumpolar Deep Water (LCDW) [21,22]. The region outlined by the orange line indicates the Prime Crust Zone defined by [12]. Topographic data are from ETOPO1 (NOAA National Geophysical Data Center; <https://www.ngdc.noaa.gov/mgg/global/>, accessed on 8 November 2021). (b) The stars indicate the locations of the sampling sites (submersible *SHINKAI 6500* dive sites) during the cruises YK10-05 (6K#1207) and YK16-01 (other dives) of the *R/V Yokosuka*. The colored fine-scale topographic data of a vessel equipped with a multiple narrow-beam echo sounder (MBES) were obtained by Nakamura et al. [24]. The white dashed line indicates the Japanese exclusive economic zone around Minamitorishima island.

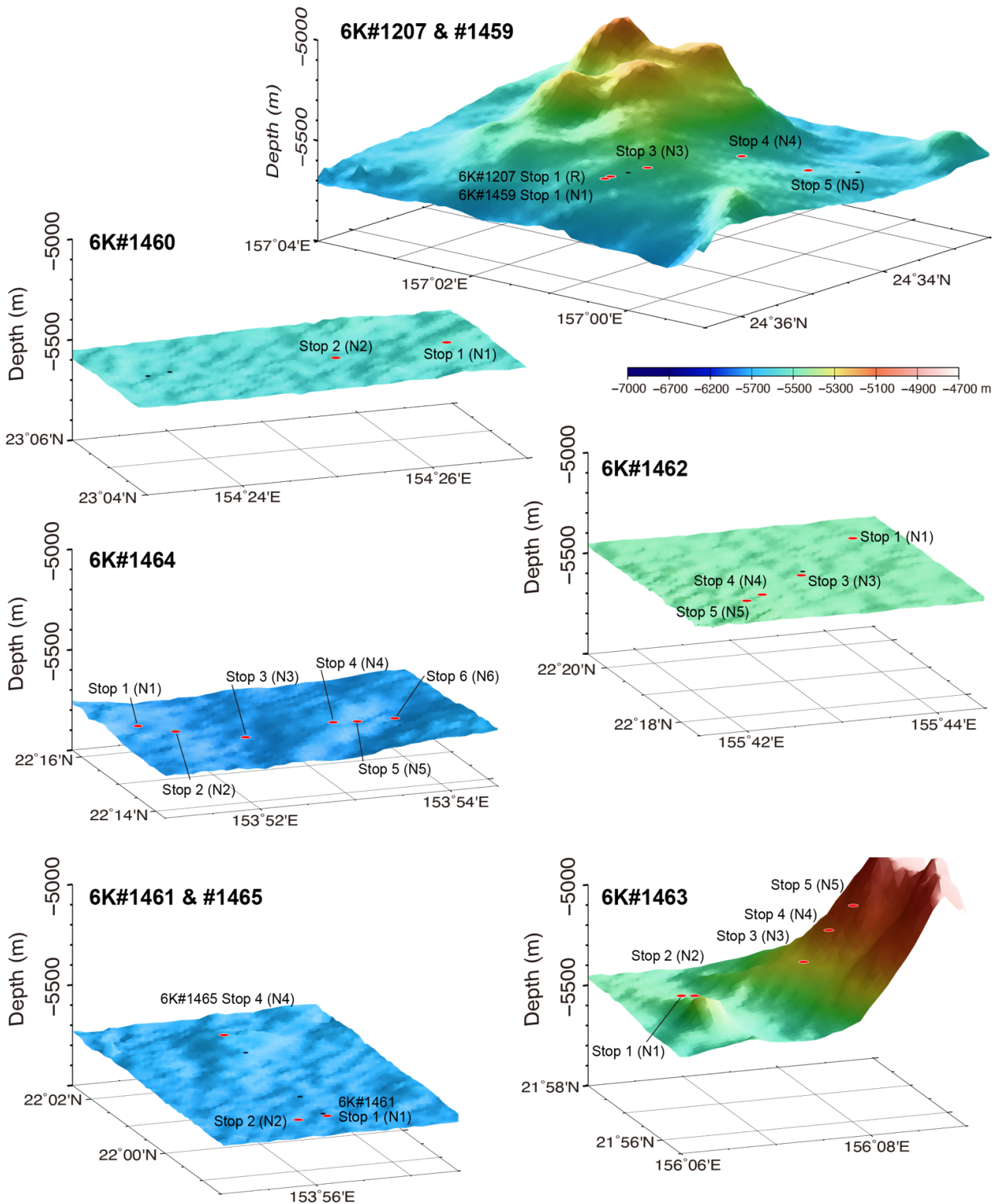


**Figure 2.** Three-dimensional maps portraying the detailed topography of the dive sites of the submersible *SHINKAI 6500* during cruise YK16-01 of *R/V Yokosuka*. Map of the sites 6K#1207 and #1459 is viewed from N40°W. The other maps are viewed from S40°W. The topographic data of a vessel equipped with MBES were compiled with the published datasets by [13]. Red circles with alphanumeric annotation indicate the stop points for detailed observation and sampling of nodules investigated in this study. The stop numbers correspond to the sample name shown in parentheses. The black dots indicate the other stop points during the same dive.

**Table 1.** Summary of sampling sites for collection of ferromanganese nodule samples, and parameters for  $\mu$ -XRF analysis.

Dive Number	Sample Name	Location			Sample Size			Analysis Parameters			
		Latitude (N)	Longitude (E)	Depth (m)	Max. (mm)	Med. (mm)	Min. (mm)	X (mm)	Y (mm)	Pixel Size ( $\mu$ m)	Total Analysis Time (ms/pixel)
6K#1459	6K#1459N1-004	24°35.69'	157°00.96'	−5501	72	71	66	71.680	71.680	140	76
	6K#1459N1-007				71	67	65	72.704	66.456	142	83
	6K#1459N1-013a				95	65	59	67.584	59.983	132	86
	6K#1459N1-013b	24°34.36'	157°00.49'	−5503	64	61	60	53.248	51.168	104	79
	6K#1459N4-001				64	61	60	62.464	61.488	122	78
	6K#1459N4-004a				34	26	14	23.552	13.392	92	162
	6K#1459N4-004b				34	26	14	31.232	16.117	122	178
6K#1459N5-002	24°33.99'	156°59.97'	−5567	63	42	40	58.368	38.874	114	172	
6K#1460	6K#1460N1-002	23°05.01'	154°26.55'	−5527	80	71	57	78.848	55.286	154	163
6K#1461	6K#1461N1-002	21°59.04'	153°56.33'	−5728	38	27	18	38.400	26.700	150	658
	6K#1461N1-005				34	30	15	34.816	14.348	136	446
	6K#1461N1-006	21°59.00'	153°56.01'	−5729	40	22	19	40.960	24.560	80	191
	6K#1461N2-013				32	20	14	29.696	15.312	116	592
6K#1462	6K#1462N1-001A	22°19.92'	155°44.06'	−5453	50	40	37	51.712	37.168	101	159
	6K#1462N1-005				60	47	44	60.416	44.014	118	84
	6K#1462N1-031				36	32	30	35.840	29.680	140	101
	6K#1462N1-038	22°18.34'	155°42.49'	−5444	35	25	20	35.840	20.440	140	94
	6K#1462N1-039				27	26	13	28.672	13.328	112	985
	6K#1462N4-001B				37	27	25	36.864	26.064	144	108
	6K#1462N5-002				89	69	48	87.040	72.760	170	91
6K#1462N5-006	22°18.17'	155°42.26'	−5443	31	24	20	31.744	22.506	124	647	
6K#1463	6K#1463N1-010	21°57.15'	156°06.65'	−5458	50	50	47	52.224	49.572	102	80
	6K#1463N1-015				28	20	19	26.112	18.972	102	105
	6K#1463N2-014				52	51	50	51.200	51.200	100	114
	6K#1463N2-019	21°57.10'	156°06.77'	−5457	26	24	24	27.648	24.084	108	105
	6K#1463N2-023				23	17	17	25.088	17.444	98	110
	6K#1463N3-007	21°56.85'	156°07.82'	−5271	45	40	38	45.568	38.448	178	543
	6K#1463N3-008				45	33	32	46.080	33.750	90	156
	6K#1463N3-016				29	26	22	29.184	26.106	114	102
	6K#1463N4-007	21°56.81'	156°08.07'	−5161	25	22	21	23.040	20.970	90	503
	6K#1463N4-009				27	22	20	28.160	21.120	110	407
	6K#1463N4-010				24	23	22	23.040	23.040	90	458
	6K#1463N5-007				21	20	19	20.992	19.188	82	92
	6K#1463N5-009	21°56.74'	156°08.30'	−5004	25	19	19	25.600	19.500	100	120
6K#1464	6K#1464N1-002	22°15.45'	153°51.38'	−5778	72	64	63	70.656	64.032	138	84
	6K#1464N1-006				62	53	52	61.440	57.000	120	82
	6K#1464N2-001	22°15.15'	153°51.66'	−5781	96	61	56	60.416	59.472	118	116
	6K#1464N3-001D				32	28	20	33.792	22.044	132	94
	6K#1464N3-008	22°14.80'	153°52.26'	−5783	39	39	37	40.448	40.132	158	461
	6K#1464N4-001				50	33	29	50.688	33.264	99	116
	6K#1464N4-010	22°14.77'	153°53.17'	−5750	41	33	32	42.240	33.990	165	347
	6K#1464N5-004				50	49	46	48.128	48.128	94	84
	6K#1464N5-011	22°14.76'	153°53.42'	−5755	53	35	30	53.248	33.800	104	84
	6K#1464N6-006				48	40	38	49.152	39.936	192	379
	6K#1464N6-007	22°14.80'	153°53.83'	−5761	44	44	43	43.008	43.008	168	458
6K#1464N6-013	33				33	32	34.816	31.756	136	117	
6K#1465	6K#1465N4-001B	22°01.67'	153°56.27'	−5679	37	36	30	37.888	29.156	148	119
	6K#1465N4-009				46	37	37	47.104	37.904	92	95
	6K#1465N4-011				48	29	17	43.520	18.190	170	88

## 2.2. Microfocus X-ray Fluorescence ( $\mu$ -XRF) Mapping

To select samples for  $\mu$ -XRF mapping, the results of the comprehensive structural observation using X-ray CT scanning [23] were carefully investigated. Nakamura et al. [23] revealed that four distinct layers, which exhibit different ranges of CT numbers (layers I, II, III, and IV) and correspond to different petrological features, are identifiable for all nodules in this region. Accordingly, we selected samples to cover the variation in nodule size and the related structural features (i.e., the number of layers obtained by the CT number criterion proposed by Nakamura et al. [23]) at an individual dive site.

Sample preparation prior to  $\mu$ -XRF mapping was conducted by the following strategy adopted by Machida et al. [13]. To create a representative cross-section for each sample, the results of the CT scanning [23] were also carefully evaluated for sample sawing. The underside (sediment side) of the nodule was recognized on the basis of sediment attachment on the surface and/or surficial structure of the ferromanganese portion, as observed in the samples taken by the push core [23]. In addition, the vertical and horizontal directions of the sample were determined and reconstructed before CT scanning. Subsequently, all samples were cut vertically; however, in the case of samples consisting of multiple nuclei, priority was given to cutting them along the cross-section through the center of all nuclei, and therefore, some samples could not be cut vertically. Subsequently, the cut surface was ground with a 120- $\mu$ m diamond disc to eliminate sawing scuff, followed by polishing with a 70- $\mu$ m diamond disc. Finally, the polished samples were allowed to dry naturally in a well-ventilated location for up to one week.

The  $\mu$ -XRF analysis was conducted at Kyoto University. The intensities of Al, Ca, Cu, Fe, K, Mg, Mn, Ni, P, Si and Ti were determined using an energy-dispersive X-ray spectrometer (EDS) attached to a  $\mu$ -XRF spectroscopy (XGT7000V; Horiba, Kyoto, Japan). The analyses were carried out following the methods described by Machida et al. [13]. Multiple measurements were conducted using a tube voltage of 50 kV, a tube current of 0.9 A, and an X-ray beam of 100  $\mu$ m in vacuo. The samples were scanned at approximately 90–178  $\mu$ m intervals (pixel size) depending on the range of the mapping area (Table 1). Intensity was determined from the cumulative intensity of the repeated analyses (more than 10 times and up to 15 times), with a total analysis time of 76–543 ms/pixel (Table 1). The analysis results were exported as TIFF-formatted files using the instrument's operation program. The elemental maps were analyzed using the Image J program.

To create a multichemical feature map of each sample, we conducted the following strategy proposed by Machida et al. [13]. At first, the Fe, Mn, Ti, P, Si, and Cu intensity maps were assigned to colored channels: green, magenta, cyan, yellow, gray, and blue, respectively. They were subsequently merged into a multi-colored map, followed by adjusting the level of each element in the merged image. As mentioned in Machida et al. [13], the Si signals were minimized, consequently improving the visualization of the fundamental ferromanganese oxide layer features and any other elemental stratigraphy.

## 3. Results

In this section, we describe the results of the layer identification of the nodules using a multichemical feature map. As defined by Machida et al. [13], the nodules from all the regions considered in this study were composed of nine common types of ferromanganese layers (Figure 3). The chemical features defining each layer were elucidated by Machida et al. [13] as follows (Figure 3): The first-order ferromanganese oxide layers (termed "L0", "L1", and "L2") were divided on the basis of Fe, Mn, and Ti content, where the outermost layer L0 was Fe-enriched (high Fe/Mn); the intermediate layer L1 exhibited high-Ti laminations; and the innermost layer L2 was Mn-enriched (low Fe/Mn). The concentration of Mn and the feature on the columnar structure of  $\delta$ -MnO<sub>2</sub> (exhibited by Mn) are the most critical proxies for defining the first-order layers. The first-order layers, L0, L1, and L2, were, respectively, subdivided into two (termed "L0 Outer" and "L0 Inner"), three (termed "L1 Outer", "L1 Middle", and "L1 Inner"), and four (termed "L2 Outermost", "L2 Outer", "L2 Middle" and "L2 Inner") layers on the basis of a combination of features

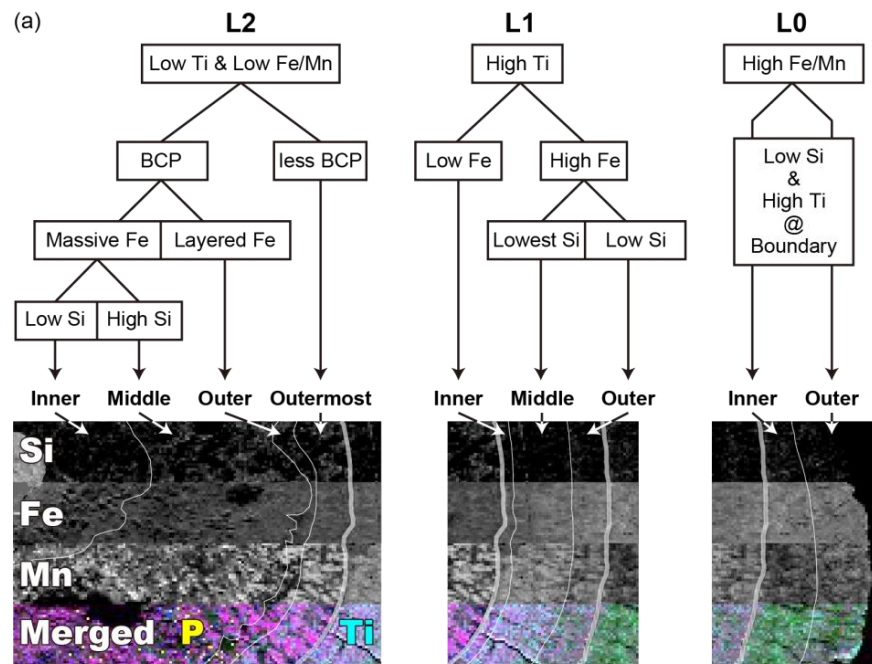
observed in the distribution of Fe, Mn, Ti, P, and Si [13] (Figure 3). As mentioned in Machida et al. [13], layer L1 might represent a key layer. In particular, we note that layer L1 Inner was easy to identify because it exhibits unique features such as high-Ti and the lowest-Si content. In contrast, a large number of small particles of biogenic calcium phosphate (BCP) (high P spots) is a useful indicator of the inner sublayers of L2 (i.e., from L2 Inner to L2 Outer). These layer definition criteria are the basis for deconvolution of the multichemical feature map. The multichemical feature maps of the representative samples are shown in Figure 4, and all samples are shown in Figures S1–S5. A summary of the layer identification process using the multichemical feature map is presented in Figure 5.

### 3.1. East and Southeast EEZ Regions

Although the innermost layer of the large nodules from sites 6K#1207 and 6K#1459 in the East EEZ region should be the layer L2 Inner, as described in Machida et al. [13,14], the multichemical feature map clearly demonstrated that several samples (e.g., 6K#1459N1-007 and 6K#1459N1-013b) lacked the layer L2 Inner (Figure 4 and Figure S1). In the case of 6K#1459N1-013 (Figure 4), the layer L0 Outer was found to envelope the outermost layers of the two different types of nodules with varying innermost layers. Some large samples are missing in the layer L1 Inner (Table 1, Figure 4, Figure 5 and Figure S1). The missing portion of the layer L0 Outer from one side (lower, sediment side) is commonly observed among the large nodules [13]. The growth of small samples collected from the deeper parts of the knoll slope (Stops 4 and 5; Figure 2) were found to have initiated from L2; however, the high-Mn layer at the L0/L1 boundary, corresponding to high Al and Si intensities, indicated that pelagic sediments are thickly wedged between L0 and L1. Moreover, it should be noted that the thicknesses of the layers L1 and L0 of these samples were thin. The smallest sample was composed of only the layer L0 Outer.

The western part of the Southeast EEZ region is represented by site 6K#1462, where it is also covered by large nodules. The multichemical feature maps indicate that although the growth of most samples had started from L2, the innermost sublayer was variable among these nodules (Table 1, Figure 4, Figure 5 and Figure S2). The layers, L2 Middle and L2 Outer, were the innermost layers of the larger nodules (e.g., N1-001 and N1-005) and the layers, L2 Outermost and L0 Outer, were found to be the innermost layers of the smaller nodules (e.g., N1-031 and N1-038). The missing portion of the layer L0 Outer from one side (lower, sediment side) was commonly observed among the larger nodules. The completely missing portions of the layers, L1 Middle and/or L1 Outermost, were observed in samples N1-038 and N5-006. The smallest sample (N1-039) was composed of only the layer L0 Outer, similar to site 6K#1459.

The size distribution of the collected nodules from site 6K#1463 in the eastern part of the Southeast EEZ region was the most variable among all the studied sites (Table 1 and Figure 5). The multichemical feature map revealed that all sublayers except the layer L1 Middle can form an innermost sublayer of nodules (Figure 4 and Figure S3). Aggregates of several nodules with the same or different innermost layers were commonly observed at site 6K#1463 (e.g., sample N3-016). The lack of sublayer(s) of L1, L2 Outermost, and L0 Outer was observed in several small nodules (e.g., N3-007). The smallest sample (N3-016b,c,d) was composed of only the layer L0 Outer, similar to the samples collected from site 6K#1459.



(b) **YK05-10 6K#1207R02**

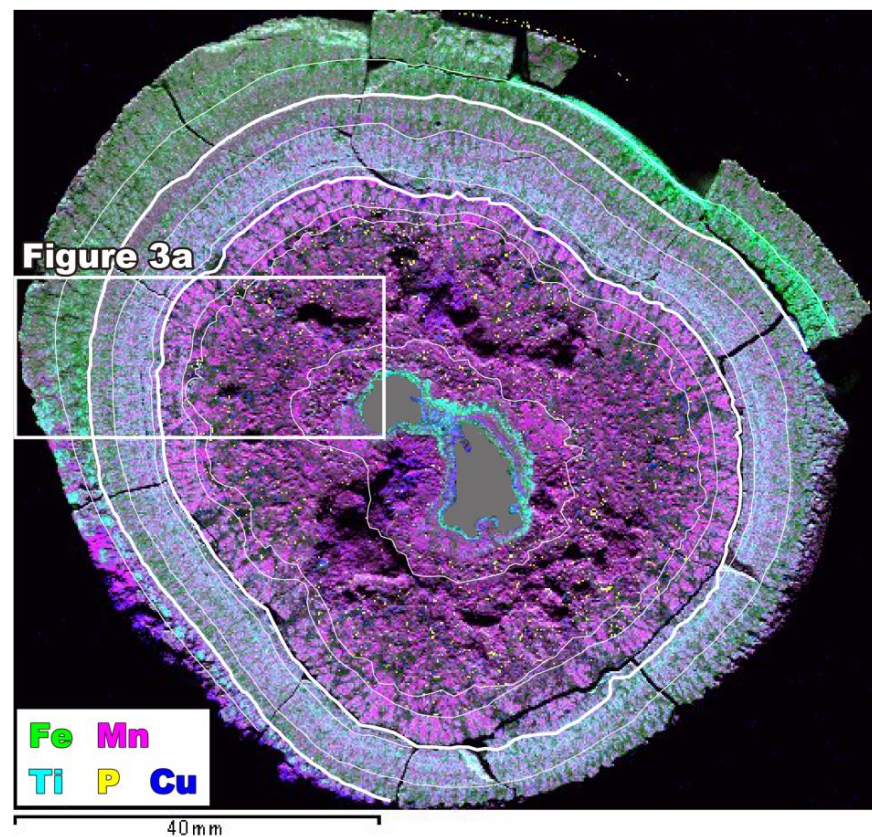
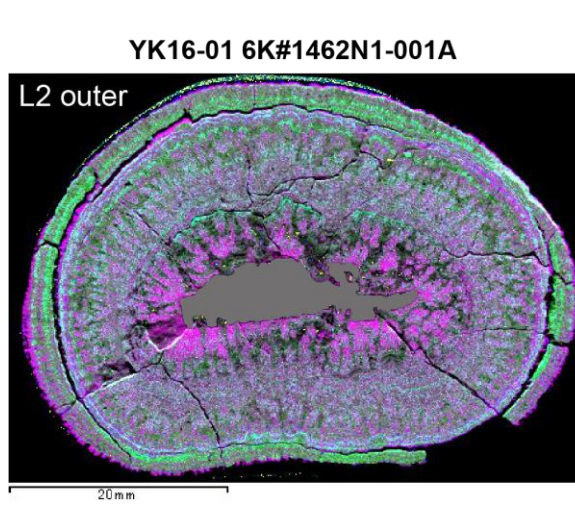
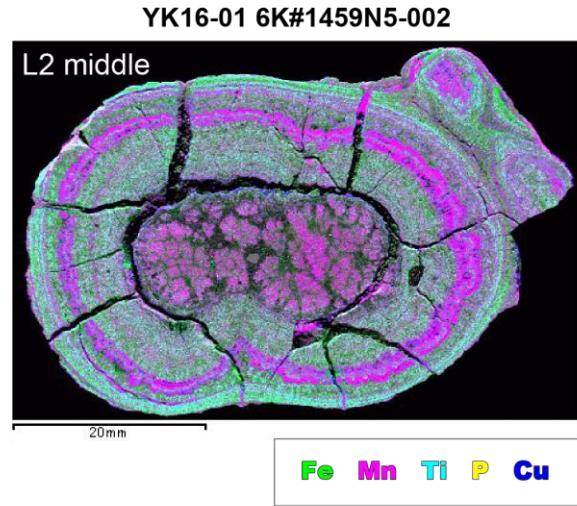
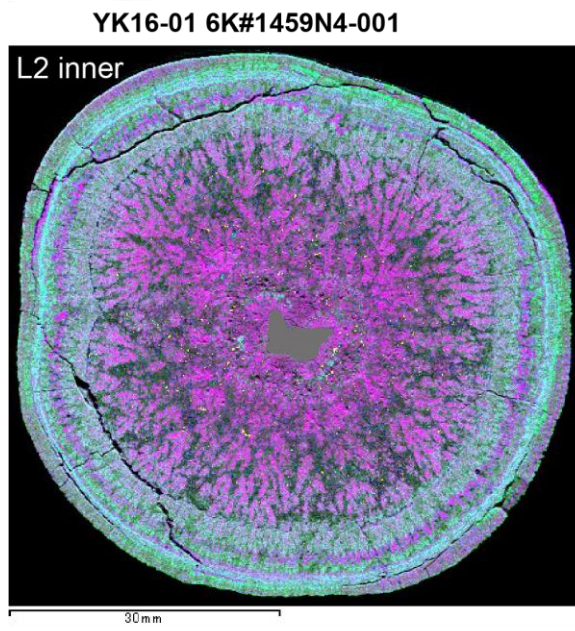
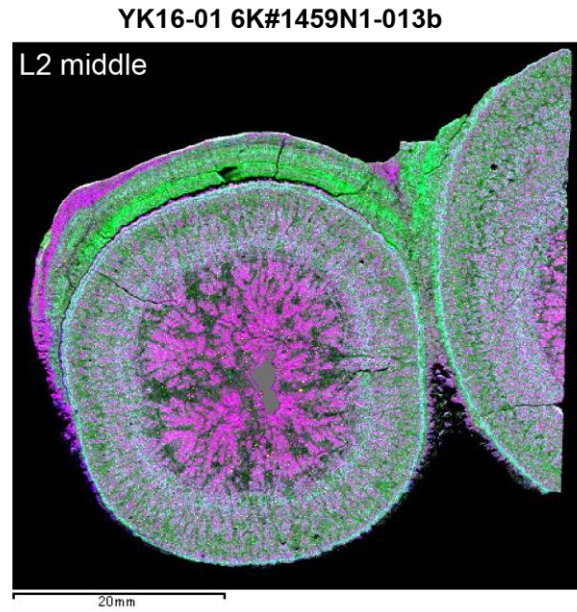
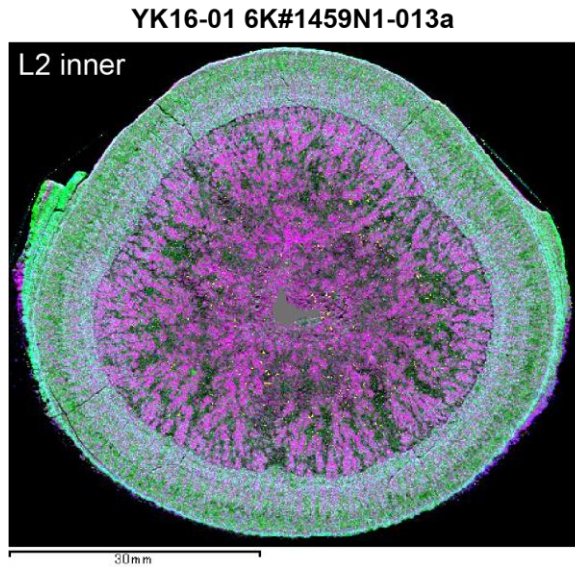


**Figure 3.** Definition criteria for chemostratigraphic layers determined by  $\mu$ -XRF. (a) Flowchart to define the sublayers proposed by Machida et al. [13] (provided in Figure 7 of [13]); (b) An example of layer identification reported by Machida et al. [13] (modified from Figure 6 of [13]). The thick white lines indicate the boundaries of the layers L0, L1, and L2, and the thin white lines indicate the sublayer boundaries of each layer. The white box in (b) indicates the area shown in (a). The gray field indicates the nuclei of this sample.

East & Southeast EEZ



YK16-01 6K#1462N1-038 YK16-01 6K#1463N2-023

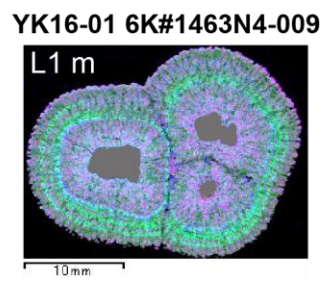
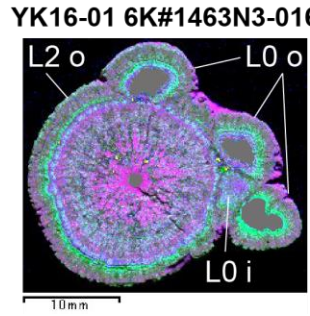
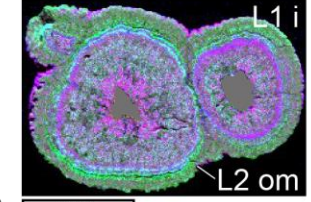
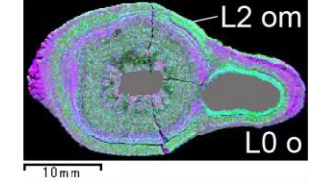
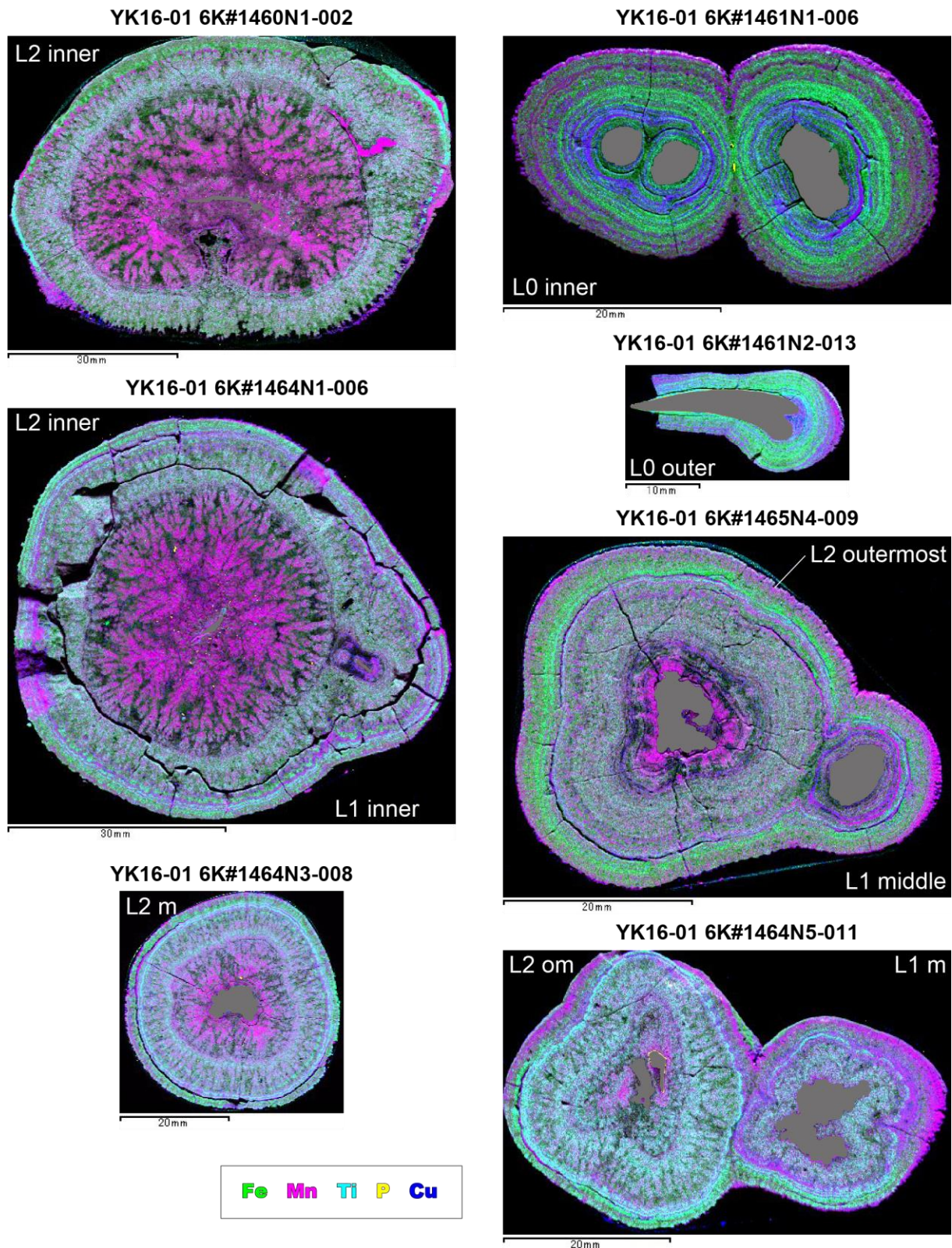


Figure 4. Cont.

**Around Takuyo Daigo SMT**



**Figure 4.** Merged multichemical feature map of the representative samples analyzed in this study. The name of the identified innermost layer around each nucleus is indicated by white text at the corner of panel. The gray field indicates the nucleus(nuclei) of each sample. i: inner; m: middle; o: outer; om: outermost.

East & Southeast EEZ

Sample Name	L2				L1			L0	
	Inner	Middle	Outer	Outer M.	Inner	Middle	Outer	Inner	Outer
6K#1207 & #1459	R02*	○	○	○	○	○	○	○	○
	N1-004	○	○	○	○	○	○	○	○
	N1-006*	○	○	○	-	○	○	○	○
	N1-007	○	○	○	○	○	○	○	○
	N1-013a	○	○	○	-	○	○	○	○
	N1-013b	○	○	○	○	○	○	○	○
	N3-001*	○	○	○	-	○	○	○	○
	N4-001	○	○	○	-	○	○	○	○
	N4-004a	○	○	○	○	○	○	○	○
	N4-004b	○	○	○	○	○	○	○	○
	N5-002	○	○	○	-	○	○	○	○
6K#1462	N1-001a	○	○	○	○	○	○	○	○
	N1-005	○	○	○	○	○	○	○	○
	N1-031	○	○	○	○	○	○	○	○
	N1-038a	○	○	○	○	○	○	○	○
	N1-038b	○	○	○	○	○	○	○	○
	N1-039	○	○	○	○	○	○	○	○
	N3-005*	○	○	○	○	○	○	○	○
	N4-001B	○	○	○	○	○	○	○	○
	N4-004*	○	○	○	-	○	○	○	○
	N5-002	○	○	○	○	○	○	○	○
	N5-006	○	○	○	-	○	○	○	○
6K#1463	N1-010	○	○	○	○	-	○	○	○
	N1-015	○	○	○	○	○	○	○	○
	N2-002*	○	○	○	○	○	○	○	○
	N2-014	○	○	○	-	○	○	○	○
	N2-019	○	○	○	○	○	○	○	○
	N2-023a	○	○	○	○	○	○	○	○
	N2-023b	○	○	○	○	○	○	○	○
	N3-002*	○	○	○	○	○	○	○	○
	N3-007a	○	○	○	-	-	-	○	○
	N3-007b	○	○	○	-	-	-	○	○
	N3-008a	○	○	○	○	○	○	○	○
	N3-008b	○	○	○	○	○	○	○	○
	N3-016a	○	○	○	○	○	○	○	○
	N3-016b	○	○	○	○	○	○	○	○
	N3-016c	○	○	○	○	○	○	○	○
	N3-016d	○	○	○	○	○	○	○	○
	N3-016e	○	○	○	○	○	○	○	○
	N4-007	○	-	-	○	○	○	○	○
	N4-009a	○	○	○	○	○	○	○	○
	N4-009b	○	○	○	○	○	○	○	○
	N4-009c	○	○	○	○	○	○	○	○
	N4-010	○	○	-	○	○	○	○	○
	N5-007	○	○	-	○	○	○	○	○
	N5-009a	○	○	○	○	○	○	○	○
	N5-009b	○	○	○	○	○	○	○	○

Around Takuyo-Daigo SMT

Sample Name	L2				L1			L0	
	Inner	Middle	Outer	Outer M.	Inner	Middle	Outer	Inner	Outer
6K #1460	N1-002	○	○	○	○	○	○	-	○
	N2-004*	○	○	○	○	○	-	○	○
6K#1464	N1-002	○	○	○	○	○	○	○	○
	N1-004*	○	○	○	○	○	○	○	○
	N1-006a	○	○	○	○	○	○	○	○
	N1-006b	○	○	○	○	○	○	○	○
	N2-001	○	○	○	○	○	○	○	○
	N3-001D	○	○	○	○	○	○	○	○
	N3-008	○	○	○	○	○	○	○	○
	N4-001a	○	○	○	○	○	○	○	○
	N4-001b	○	○	○	○	○	○	○	○
	N4-004*	○	○	○	○	○	○	○	○
	N4-010	○	○	○	○	○	○	○	○
	N5-004	○	○	○	○	○	○	○	○
	N5-011a	○	○	○	○	○	○	○	○
	N5-011b	○	○	○	○	○	○	○	○
	N5-006	○	○	○	○	○	○	○	○
	N6-007	○	○	○	○	○	○	○	○
	N6-013	○	○	○	○	○	○	○	○
6K#1461	N1-002a	○	○	○	○	○	○	○	○
	N1-002b	○	○	○	○	○	○	○	○
	N1-002c	○	○	○	○	○	○	○	○
	N1-002d	○	○	○	○	○	○	○	○
	N1-005	○	○	○	○	○	○	○	○
	N1-006	○	○	○	○	○	○	○	○
	N2-013	○	○	○	○	○	○	○	○
6K#1465	N4-001Ba	○	○	○	○	○	○	○	○
	N4-001Bb	○	○	○	○	○	○	○	○
	N4-009a	○	○	○	○	○	○	○	○
	N4-009b	○	○	○	○	○	○	○	○
	N4-011	○	○	○	○	○	○	○	○

**Figure 5.** Observed layers for each sample collected from the nodule field around Minamitorishima Island. In this figure, the sites are arranged from north (upper) to south (lower) in each region. The identified sublayers in all samples, including samples previously reported by [13] and the samples shown as '\*' with the sample name, are indicated by circles (O) in each box. Layer identification is based on both  $\mu$ -XRF mapping (the merged multichemical feature map) of the samples and the definition of each sublayer proposed by [13] (Figure 3). The box marked by '-' indicates the complete absence of the sublayer. The gray bar corresponds to the nuclei shown in Figure 4 and Figures S1–S5 to easily recognize the innermost layer of each sample. The alphabet 'a', 'b', 'c', 'd', and 'e' with the sample name indicate the samples consisting of multiple nuclei or aggregates of several nodules.

3.2. Around Takuyo Daigo Seamount Region

During diving at site 6K#1460 in the northern part of the Around Takuyo Daigo Seamount region, we collected several large nodules using a manipulator. Sample N1-002 is characterized by the layer L2 Inner as the innermost layer, in contrast to sample N2-004 reported by Machida et al. [13]. The complete absence of the layer L1 Outer and the missing portion of the layer L0 Outer from one side (lower, sediment side) of the nodule were observed in both the samples. The latter is also a feature of large samples from sites 6K#1459 (6K#1207) and 6K#1462, as mentioned in Section 3.1.

Site 6K#1464 had the most variable size distribution of the nodules in this region (Table 1 and Figure 5). As shown by the multichemical feature map, such a variable size distribution was regulated by differences in the innermost layer of the sublayers of L2 (Figure 4 and Figure S5). The innermost layers of the nodules at this site were identified at all sublayers except for the layer L2 Outer. Interestingly, the layer L2 Inner was only observed in samples from the western part of the survey track line of dive 6K#1464 (Stop 1), and the innermost layer of the nodule changed progressively from the inner to the outer layer along the eastward track line from Stop 1 to Stop 6 (Figure 5 and Figure S5).

Site 6K#1461 is located in the low acoustic backscatter intensity region, where small nodules distribute sparsely [5]. The innermost layer of most small nodules from Stops 1 and 2 of site 6K#1461 was the layer L0 Outer (Table 1, Figure 4, Figure 5 and Figure S4). A nodule with the innermost layer being the layer L0 Inner was rarely sampled from Stop 1. In contrast to site 6K#1461, we observed that large nodules were sparsely distributed at site 6K#1465, which is the top of the small mound at approximately three km north of site 6K#1461 (Figure 2). Although the innermost layer of the small nodules from site 6K#1465 (N4-001 and N4-011) was the layer L0 Inner or Outer, as with those from site 6K#1461, the larger nodules from site 6K#1465 (N4-009) mostly had the layers, L2 Outermost or L1 Middle.

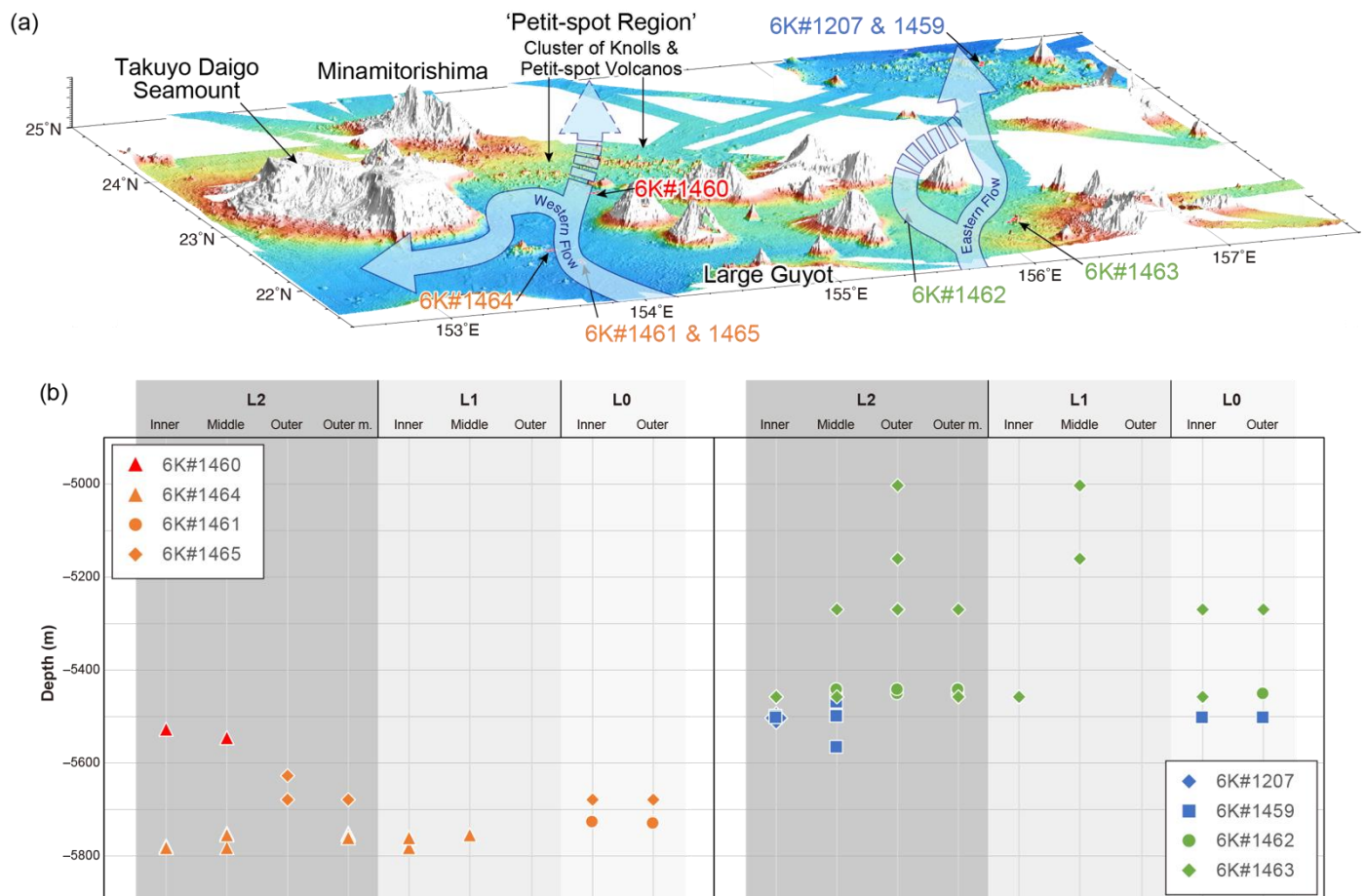
#### 4. Discussion

Figure 5 shows that all the sublayers, except the layer L1 Outer, are identified as the innermost layer of nodules distributed in this area. It is thought that a low sedimentation rate owing to the higher bottom current velocities is an important factor of growth of the ferromanganese layers [3,4]. Therefore, the different chemical characteristics of each sublayer imply that the chemistry of the deep-sea water mass that formed the hydrogenous nodules and crust had temporally changed in the study region [13]. Each sublayer of a nodule can be regarded as an isochronous plane of growth history from around a nucleus to the surface; however, since the combination of the innermost layers varied from site to site, we consider that there are regional variations on timing for the growth initiation of nodules.

Upon dividing the nodule field into northern (6K#1207/1459 in the East EEZ region and 6K#1460 in the Around Takuyo Daigo Seamount region) and southern (6K#1462 and 6K#1463 in the Southeast EEZ region, and 6K#1464 and 6K#1461/1465 in the Around Takuyo Daigo Seamount region) sides, we found that the variation in the innermost layer was larger on the southern side of the field in each region compared to that on the northern side (Figure 5). Our data further indicated that the formation of nodules in the northern side of the field started at the stage when the layers, L0 Inner and Outer, occurred solely on the eastern side of the field (6K#1207/1459). This implies that the beginning of nodule formation occurred more frequently at the south of each region. Therefore, we consider that the deep-sea current always flowed into the region from the southern direction, and that it passed between the seamounts to the northern direction (Figure 6). Consequently, a field of large nodules was formed by the continuous growth of each ferromanganese oxide sublayer with different chemical composition characteristics. The distribution density of nodules was intermittently increased particularly in the southern part of the vast field.

Furthermore, our detailed examination revealed different patterns of nodule formation in each eastern or western region, which is described as follows. In the Southeast EEZ region, nodules with the layer L1 as the innermost layer were present at site 6K#1463, and not at site 6K#1462. This suggests that the western side, where the adjacent seamounts are close, is less prone to ocean currents. Deep-sea currents always characterize the flow line toward the eastern side; however, as discussed earlier, additional nodule formation at site 6K#1270/1459 in the northern part of the nodule field (the East EEZ region) is rare. On the other hand, in the Around Takuyo Daigo Seamount region, the nodule formation started at the L2 stage at site 6K#1460, which corresponds to the southern end of the region where there are several knolls [25]. However, in the L1 stage, the additional nodule formation was limited at site 6K#1464, and it was negligible at site 6K#1460. Hirano et al. [25] reported that one knoll in the region north of site 6K#1460 was formed by petit-spot volcanism (hereafter referred to as the ‘petit-spot region’; Figure 6). Furthermore, Machida et al. [5] reported that the acoustic backscatter intensity decreases from the petit-spot region to the north (the eastern region off Minamitorishima), indicating that the nodule density area does not extend downstream of the deep-sea current. Thus, we considered that the mainstream deep-sea current in this region turned westward in the south of the petit-spot region and subsequently flowed northwestward, thereby avoiding the Takuyo Daigo

Seamount. Indeed, a high reflection intensity area extends to the southeast of the Takuyo Daigo seamount, and the distribution of nodule-dense areas has been confirmed [5]. In the future, it is necessary to conduct the same analysis that has been conducted in this study in nodules collected from regions surrounding the Takuyo Daigo Seamount, to clarify the western flow path of deep-sea currents.



**Figure 6.** Expected flow direction of deep-sea currents that had intermittently supplied materials to be the nuclei of nodules in the regions around Minamitorishima Island. (a) Three-dimensional map portraying detailed topography and sampling sites viewed from S40°W. Bathymetric data and the color scale as same as in Figure 2. (b) Relationships between depth of sampling site (Table 1 and Figure 2) and the innermost layer (i.e., layer around the nuclei) of each different-sized nodule (Figure 5).

Kawabe et al. [20] reported that the mainstream of the DWBC gets bifurcated by a large seamount situated at 15° N and 155° E (Figure 1a). The eastern bifurcated current flows toward the Minamitorishima EEZ, and further flows from southeast to southwest in the southern direction of our study area (Figure 1a; [21,22]). Figure 1b shows that a large guyot is situated at the southern tip of the Minamitorishima EEZ (21° N and 155° E). Therefore, we consider that this guyot can further bifurcate the eastern current to form two smaller magnitude branch currents of the DWBC. Indeed, as discussed earlier, the deep-sea currents flowing in the studied area are divided into two flows: one flows from the south through the Southeast EEZ region to the East EEZ region on the eastern side of the study area (the eastern flow), and the other flows from the south into the Around Takuyo Daigo Seamount region and outward toward the northwestward direction (the western flow). Accordingly, we propose that the headwaters of both flows in this region were originated from the LCDW, and the two flows obtained in this study (the eastern and western flows; Figure 6) belong to the small-scale branched LCDW. On the other hand, our

results indicate that the deep-sea currents in the studied area followed similar routes in the past. Therefore, we can suggest that the arrangement of individual seamounts strongly regulates the flow path of the LCDW, even if the position of the entire group of seamounts might have changed due to plate motion. We note a fact never recognized before that even the cluster of small petit-spot volcanoes (knolls) could provide a critical constraint on the flow path of deep-sea currents.

Figure 6 shows the relationship between water depth and the timing of the initiation of nodule growth at each sampling site. We found that nodule formation started at a shallow depth at site 6K#1463 during the stage of the L2 of the eastern flow. Moreover, the range of depth seems to have gradually increased to the stage of the layer L2 Outer, and subsequently decreased to the later stage. These observations suggest that the flow volume is larger than that of the other stages of the L2; however, since there is no information on the shallow water depth of the western flow, it is not clear whether the relationship between the depth and the timing of nuclei supply in the eastern flow is common in the Minamitorishima EEZ region. Further systematic sampling and analyses are required to confirm this relationship.

For the initiation of ferromanganese nodule growth, the nucleus, which is mainly composed of clay lumps, rock chips, fish teeth, other skeletal remains, and fragments of older nodules and crust, is essential [3]. Therefore, our lines of discussion can propose a hypothesis that the materials to be the nuclei of the nodules were supplied every time the water mass of the LCDW switched and a new deep-sea current entered the regions. As a result, a vast area densely covered by ferromanganese nodules was formed. Future studies in other nodule fields are required to verify whether our hypothesis is applicable to explain the geology of the field and the relationship between the distribution of the nodule field and deep-sea current, which is essentially regulated by the topographic framework of the seafloor.

We conducted nondestructive fine-scale inter-structural observations of hydrogenous ferromanganese nodules using  $\mu$ -XRF analysis. An important point of our analysis is that the systematic sample selection was based on comprehensive observation using CT. Our results provide essential information for examining the nuclei supply and oxide layer growth processes in terms of the oceanography of deep-sea currents. Such a multidisciplinary analysis for the other nodule fields and the ferromanganese crust on the seamounts has the potential to critically constrain the complex relationship between the formation of ferromanganese oxides, the temporal and global-scale evolution of the LCDW, and the deep-sea environment.

## 5. Conclusions

A  $\mu$ -XRF analysis was conducted to define the chemostratigraphy of hydrogenous ferromanganese nodules distributed in the regions from the southern to the eastern part of the Minamitorishima EEZ. Based on the results, eight types of sublayers (L2 Inner, L2 Middle, L2 Outer, L2 Outermost, L1 Inner, L1 Middle, L0 Inner, and L0 Outer), previously defined by Machida et al. [13], were identified as the innermost layers of nodules in the study area. This indicates that the intermittent initiation of nodule formation and the resulting increase in the number of nodules lead to both wider spreading across the field and denser growth within the field. Moreover, the type of the innermost layer was more variable in samples from the southern part of the study area than in those from the northern part. These facts are consistently explained by the following hypothesis: (1) the materials to be the nucleus of the nodules were supplied every time the water mass switched, and a new deep-sea current entered the regions from the south; (2) the deep-sea current originated from the LCDW; and (3) the nodules began to grow owing to the participation of source materials/elements from an oxic deep-sea current to form hydrogenous ferromanganese layers around the nuclei/nucleus. We expected that the two small-scale branched LCDWs were bifurcated by a large guyot at 21° N and 155° E and flowed separately into the western and eastern

regions of the study area. This further suggests that topography strongly regulates the flow path of the deep-sea current through the time of nodule growth.

**Supplementary Materials:** The following are available online at <https://www.mdpi.com/article/10.3390/min11111246/s1>, Figure S1: Merged multichemical feature map of the samples analyzed in this study collected from site 6K#1459 in the East EEZ region during the cruise YK16-01. Figure S2: Merged multichemical feature map of the samples analyzed in this study collected from site 6K#1462 in the Southeast EEZ region during the cruise YK16-01. Figure S3: Merged multichemical feature map of the samples analyzed in this study collected from site 6K#1463 in the Southeast EEZ region during the cruise YK16-01. Figure S4: Merged multichemical feature map of the samples analyzed in this study collected from sites 6K#1460, 6K#1461, and 6K#1465 in the Around Takyo Daigo Seamount. Figure S5: Merged multichemical feature map of the samples analyzed in this study collected from site 6K#1464 in the Around Takyo Daigo Seamount region during the cruise YK16-01.

**Author Contributions:** Conceptualization, S.M. and K.N.; methodology, S.M., K.N. and T.K.; formal analysis, S.M., R.S. and T.K.; investigation, S.M. and R.S.; resources, S.M.; data curation, S.M.; writing—original draft preparation, S.M.; writing—review and editing, all authors; visualization, S.M. and R.S.; supervision, Y.K.; project administration, S.M.; funding acquisition, S.M., K.N. and Y.K. All authors have read and agreed to the published version of the manuscript.

**Funding:** This research was funded by the cross-ministerial Strategic Innovation Promotion Program (SIP) of Japan and JSPS through the Grant-in-Aid Scientific Research (S) No. 15H05771, (A) No.17H01361, and (A) No.21H04667.

**Data Availability Statement:** Data are shown in all figures and tables of the main text and in the Supplementary Materials. Raw data and compositional map of each analyzed elements (Al, Ca, Cu, Fe, K, Mg, Mn, Ni, P, Si and Ti) using  $\mu$ -XRF can be provided from the corresponding author upon request.

**Acknowledgments:** We gratefully acknowledge the captains, crews and shipboard scientific parties of the *R/V Yokosuka*, and operating team of the *SHINKAI 6500* for their efficient work during the cruise YK16-01. The research cruise was conducted in the SIP of Japan.

**Conflicts of Interest:** The authors declare no conflict of interest. The funders had no role in the design of the study; in the collection, analyses, or interpretation of data; in the writing of the manuscript, or in the decision to publish the results.

## References

1. Hein, J.R.; Petersen, S. The geology of manganese nodules. In *Deep Sea Minerals: Manganese Nodules: A Physical, Biological, Environmental and Technical Review*; Baler, E., Beaudoin, Y., Eds.; Secretariat of the Pacific Community: Noumea, New Caledonia, 2013; Volume 1B, pp. 7–18.
2. Hein, J.R.; Koschinsky, A.; Kuhn, T. Deep-ocean polymetallic nodules as a resource for critical materials. *Nat. Rev. Earth Environ.* **2020**, *1*, 158–169. [[CrossRef](#)]
3. Glasby, G.P.; Stoffers, P.; Sioulas, A.; Thijssen, T.; Friedrich, G. Manganese nodule formation in the Pacific Ocean: A general theory. *Geo-Marine. Lett.* **1982**, *2*, 47–58. [[CrossRef](#)]
4. Nishimura, A. Sedimentation and hiatuses in the Central Pacific basin: Their relationship to manganese nodule formation. In *Geology and Offshore Mineral Resources of the Central Pacific Basin*; Keating, B.H., Bolyon, B.R., Eds.; Circum-Pacific Council for Energy and Mineral Resources, Earth Sciences Series; Springer: Berlin/Heidelberg, Germany, 1992; Volume 14, pp. 179–203.
5. Machida, S.; Sato, T.; Yasukawa, K.; Nakamura, K.; Iijima, K.; Nozaki, T.; Kato, Y. Visualisation method for the broad distribution of seafloor ferromanganese deposits. *Mar. Georesour. Geotechnol.* **2021**, *39*, 267–279 (published on line in 2019). [[CrossRef](#)]
6. Sorem, R.K.; Reinhart, W.R.; Fewkes, R.H.; McFarland, W.D. Occurrence and character of manganese nodules in DOMES Sites A, B, and C, east equatorial Pacific Ocean. In *Marine Geology and Oceanography of the Pacific Manganese Nodule Province*; Bischoff, J.L., Piper, D.Z., Eds.; Plenum Publishing Corp.: New York, NY, USA, 1979; pp. 475–527.
7. Heath, G.R. Burial rates, growth rates, and size distributions of deep-sea manganese nodules. *Science* **1979**, *205*, 903–904. [[CrossRef](#)] [[PubMed](#)]
8. Usui, A. Regional variation of manganese nodules facies on the Wake-Tahiti transect: Morphological, chemical and mineralogical study. *Mar. Geol.* **1983**, *54*, 27–51. [[CrossRef](#)]
9. Bolton, B.R.; Bogi, J.; Cronan, D.S. Geochemistry and Mineralogy of ferromanganese nodules from the Kiribati region of the Eastern Central Pacific. In *Geology and Offshore Mineral Resources of the Central Pacific Basin*; Keating, B.H., Bolyon, B.R., Eds.; Circum-Pacific Council for Energy and Mineral Resources, Earth Sciences Series; Springer: Berlin/Heidelberg, Germany, 1992; Volume 14, pp. 247–260.

10. Kuhn, T.; Wegorzewski, A.; Rühlemann, C.; Vink, A. Composition, Formation, and Occurrence of Polymetallic Nodules. In *Deep-Sea Mining*; Sharma, R., Ed.; Springer: Berlin/Heidelberg, Germany, 2017; pp. 23–63.
11. Hein, J.R.; Conrad, T.A.; Dunham, R.E. Seamount characteristics and mine-site model applied to exploration and mining-lease-block selection for cobalt-rich ferromanganese crusts. *Mar. Georesour. Geotechnol.* **2009**, *27*, 160–176. [[CrossRef](#)]
12. Hein, J.R.; Mizell, K.; Koschinsky, A.; Conrad, T.A. Deep-ocean mineral deposits as a source of critical metals for High and green-technology applications: Comparison with land-based resources. *Ore Geol. Rev.* **2013**, *51*, 1–14. [[CrossRef](#)]
13. Machida, S.; Nakamura, K.; Kogiso, T.; Shimomura, R.; Horinouchi, K.; Okino, K.; Kato, Y. Fine-scale chemostratigraphy of cross-sectioned hydrogenous ferromanganese nodules from the western North Pacific. *Isl. Arc* **2021**, *30*, e12395. [[CrossRef](#)]
14. Machida, S.; Fujinaga, K.; Ishii, T.; Nakamura, K.; Hirano, N.; Kato, Y. Geology and geochemistry of ferromanganese nodules in the Japanese Exclusive Economic Zone around Minamitorishima Island. *Geochem. J.* **2016**, *50*, 539–555. [[CrossRef](#)]
15. Kim, J.; Hyeong, K.; Yoo, C.M.; Moon, J.W.; Kim, K.H.; Ko, Y.T.; Lee, I. Textural and geochemical characteristics of Fe-Mn crusts from four seamounts near the Marshall Islands, western Pacific. *Geosci. J.* **2005**, *9*, 331–338. [[CrossRef](#)]
16. Kim, J.; Hyeong, K.; Jung, H.-S.; Moon, J.-W.; Kim, K.-H.; Lee, I. Southward shift of the Intertropical Convergence Zone in the western Pacific during the late Tertiary: Evidence from ferromanganese crusts on seamounts west of the Marshall Islands. *Paleoceanography* **2006**, *21*, PA4218. [[CrossRef](#)]
17. Pan, J.; De Carlo, E.H.; Yang, Y.; Liu, S.; You, G. Effect of phosphatization on element concentration of cobalt-rich ferromanganese crusts. *Acta Geol. Sin.* **2005**, *79*, 349–355.
18. Nozaki, T.; Tokumaru, A.; Takaya, Y.; Kato, Y.; Suzuki, K.; Urabe, T. Major and trace element compositions and resource potential of ferromanganese crust at Takuyo Daigo Seamount, northwestern Pacific Ocean. *Geochem. J.* **2016**, *50*, 527–537. [[CrossRef](#)]
19. Azami, K.; Hirano, N.; Machida, S.; Yasukawa, K.; Kato, Y. Rare earth elements and yttrium (REY) variability with water depth in hydrogenetic ferromanganese crusts. *Chem. Geol.* **2018**, *493*, 224–233. [[CrossRef](#)]
20. Kawabe, M.; Fujio, S.; Yanagimoto, D. Deep-water circulation at low latitudes in the western North Pacific. *Deep-Sea Res. I Oceanogr. Res. Pap.* **2003**, *50*, 631–656. [[CrossRef](#)]
21. Kawabe, M.; Fujio, S.; Yanagimoto, D.; Tanaka, K. Water masses and currents of deep circulation southwest of the Shatsky Rise in the western North Pacific. *Deep-Sea Res. I Oceanogr. Res. Pap.* **2009**, *56*, 1675–1687. [[CrossRef](#)]
22. Kawabe, M.; Fujio, S. Pacific Ocean circulation based on observation. *J. Oceanogr.* **2010**, *66*, 389–403. [[CrossRef](#)]
23. Nakamura, K.; Terauchi, D.; Shimomura, R.; Machida, S.; Yasukawa, K.; Fujinaga, K.; Kato, Y. Three-dimensional structural analysis of ferromanganese nodules from the western North Pacific Ocean using X-ray Computed Tomography. *Minerals* **2021**, *11*, 1100. [[CrossRef](#)]
24. Nakamura, K.; Machida, S.; Okino, K.; Masaki, Y.; Iijima, K.; Suzuki, K.; Kato, Y. Acoustic characterization of pelagic sediments using sub-bottom profiler data: Implications for the distribution of REY-rich mud in the Minamitorishima EEZ, western Pacific. *Geochem. J.* **2016**, *50*, 605–619. [[CrossRef](#)]
25. Hirano, N.; Machida, S.; Sumino, H.; Shimizu, K.; Tamura, A.; Morishita, T.; Iwano, H.; Sakata, S.; Ishii, T.; Arai, S.; et al. Petit-spot volcanoes on the oldest portion of the Pacific plate. *Deep-Sea Res. I Oceanogr. Res. Pap.* **2019**, *154*, 103142. [[CrossRef](#)]